Activation-relaxation technique study of two-level system impact on internal dissipation using DFT-based moment tensor potential

Renaude Girard,[*] Carl Lévesque, Normand Mousseau,[†] and François Schiettekatte[‡]
Département de Physique, Institut Courtois and Regroupement Québécois sur les Matériaux de Pointe, Université de Montréal, C.P. 6128, Succursale Centre-Ville, Montréal, Québec, Canada H3C 3J7

(Received 24 November 2025; accepted 15 April 2026; published 6 May 2026)

We use a recently developed machine-learned moment tensor potential (MTP) trained on data generated with the density functional theory and tailored to amorphous silicon coupled with the activation-relaxation technique nouveau (ARTn) to identify and classify two-level systems (TLSs). The samples generated using MTP recover experimental results and provide average structural and dissipative properties similar to those obtained with a modified Stillinger-Weber potential, including radial distribution function, defect concentration, and internal friction. Atomistic details, however, are significantly different, including the density and type of TLS. In particular, we find that while the density of the TLS involving a bond-hopping mechanism is similar for the two potentials, more complex TLSs, such as those involving a Wooten-Winer-Weaire bond exchange, are about twice as common. Analysis also shows that TLSs, for MTP-based models, are mostly isolated and oscillate independently from each other.

DOI: 10.1103/9g5j-9q4n

I. INTRODUCTION

After 10 years of operation since the first detection, large-scale gravitational wave detectors (GWDs) have led to the observation of hundreds of gravitational waves [1], confirming so far Einstein's general theory of gravitation [2]. These detectors are based on a Michelson interferometer with arms a few kilometers long, each containing a Fabry-Perot cavity [3]. With current detectors, events involving compact objects, for example, the collision of two black holes, can be identified reliably. However, the detection of events involving smaller or more distant masses, with sufficient precision to characterize them, is limited by the background noise. In order to access and characterize those events, considerable efforts were spent in the comprehension and identification of the sources of the background noise.

For current GWD experiments, the sensitivity is optimal around 100 Hz [4]. At this frequency, the main sources of noise come from fluctuations in mirror coating and quantum noise [5]. Analysis based on the fluctuation-dissipation theory [6] shows that the coating thermal noise originates from microscopic mechanical fluctuations around local configurational minima, which can be attributed to classically activated atomic-scale two-level systems (TLSs) [7]. TLSs correspond to systems composed of two close-by local metastable states of similar energy separated by a relatively low-energy barrier. Although the general description of TLSs was provided many decades ago, the mechanistic details, which may depend closely on the specificity of the materials, are still lacking, hence a handle on ways to control them. Special focus has been given to TiO_2:Ta_2O_5 [8,9] and SiO_2, the former being the high index material in the current GWD reflective stacks and the one contributing the most to the coating thermal noise, while the latter is the low index material and one of the amorphous materials with the lowest internal dissipation at room temperature [10].

Amorphous silicon (*a*-Si) also features a low internal dissipation [11] hence low noise, while it has a high refractive index; its incorporation in optical stacks for GWD is a subject of active research [12–14]. Recently, atomistic mechanisms responsible for the mechanical loss associated with TLSs were identified in models of *a*-Si described with the empirical modified Stillinger-Weber potential (mSW) [15] using an open-ended transition state search method, the *activation-relaxation technique nouveau* (ARTn) [16]. As *a*-Si is a mono-atomic amorphous material and a potential candidate for the next generation of GWD mirrors [17], this characterization offered both generic information on the atomistic origin of TLSs and specific details on dissipation mechanisms in a potentially relevant material. While this study provided a coherent picture of TLSs that is in general agreement with experimental dissipation measurements, it suffers from the use of an empirical potential that was fitted to reproduce the overall structural properties of *a*-Si, but not its dynamical properties. Indeed, as shown, for example, in Ref. [18], transition-state configurations generated with this potential in an ion-implanted crystalline silicon simulation box may not correspond to barriers predicted with density functional theory (DFT).

Since the concentration of TLSs in *a*-Si is low, their study requires accumulating considerable statistics on simulation cells too large to be explored using DFT approaches. With recent advances in machine learning, it is now possible to circumvent this barrier using rich machine-learned potentials (MLPs) that are fitted with high precision to DFT calculations

[*]Contact author: renaud.girard@umontreal.ca
[†]Contact author: normand.mousseau@umontreal.ca
[‡]Contact author: francois.schiettekatte@umontreal.ca

[19]. Contrary to DFT, these MLPs are localized in nature and, therefore, scale well with system size, while providing a precise physical description at accessible computational costs. In this work, we reexamine the fundamental nature of the atomistic mechanisms responsible for TLSs in *a*-Si using a recently developed high-quality universal MLP for Si based on the moment-tensor potential formalism [20] fitted to DFT calculations [21]. We also compare our results with both experiments and recent modeling efforts using a purely empirical potential, which allows us to compare a well-established empirical potential directly to an MLP in the context of a complex structure. We identify subtle but notable differences in the geometrical details of TLSs that might impact strategies to handle those for gravitational wave detection, for example.

This paper is constructed as follows. We first present a brief overview of TLSs before describing the modeling approach and the analysis methods. We then present results and compare with TLSs generated with empirical potentials, showing that the MLP-based models find twice as many defects as the empirical potential, although the mechanisms identified are more compact and complex.

II. THEORY AND METHODS

This section provides a short introduction to TLSs and to the generation and analysis methods used to explore TLSs in realistic models of *a*-Si.

A. Two-level systems

The time evolution of a mechanical system can be described as a series of thermally activated events. Each event involves a transition from a metastable state to another through a trajectory characterized by an energy barrier defined at the first-order transition state. While, in disordered systems, these energy barriers can be associated with a broad energy spectrum, events contributing to the background noise in GWD correspond to a small subset of these events, associated with TLSs, which are characterized by oscillations between two states of similar energy with a barrier corresponding to frequencies between 10 and 10 000 Hz.

More specifically, a TLS consists of a system of two minima separated by a low-energy single saddle point and surrounded by significantly higher energy barriers, effectively creating an isolated two-state basin (see Fig. 1).

A TLS is characterized by the energy asymmetry, $\Delta = |E_b - E_a|$, and the mean barrier energy,

$$V = \frac{E_S - E_a}{2} + \frac{E_S - E_b}{2}, \tag{1}$$

between the two metastable minima of energy E_a and E_b.

In the transition-state theory [22], we use the Arrhenius law to find the mean rate of transition between two minima in the potential plane. Neglecting quantum tunneling,

$$\tau_{i\to j} = \tau_0 e^{\frac{E_{\text{sad}} - E_i}{k_b T}}, \tag{2}$$

where $\tau_{i\to j}$ is the average time between transitions from minimum i to minimum j, E_{sad} is the energy at the barrier between i and j, k_b is the Boltzmann constant, T is the temperature, and τ_0^{-1} is the attempt frequency of the event.

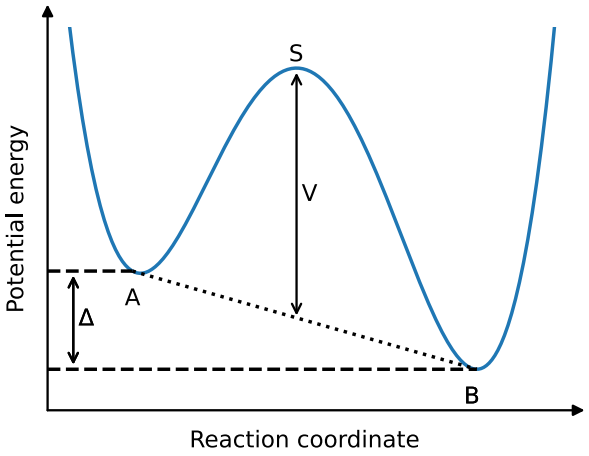

FIG. 1. Representation of the configurational energy of a TLS as a function of its reaction coordinate. This TLS consists of two minima, A and B, separated by a saddle point S surrounded by high-energy barriers. Δ indicates the asymmetry between the two minima and V the mean energy barrier.

The contribution of TLSs to the background noise can be computed as the loss angle, which treats each TLS in a symmetric fashion between states a and b,

$$Q^{-1}(\omega) = \frac{1}{\mathcal{V}C} \sum_{i,\text{TLS}} \frac{\gamma_i^2}{k_b T} \frac{\omega\tau_i}{1+\omega^2\tau_i^2} \text{sech}^2\left(\frac{\Delta_i}{2k_b T}\right), \tag{3}$$

which can be measured experimentally, where τ_i, the relaxation time, is given by

$$\tau_i = \tau_0 \text{sech}\left(\frac{\Delta_i}{2k_b T}\right) e^{\frac{V_i}{k_b T}}. \tag{4}$$

Here, C is the elastic modulus (longitudinal or transverse), γ_i is the deformation potential, and $\mathcal{V}$ the volume of the system.

The full derivation for these equations is given in Ref. [7]. The coupling tensor $\bar{\gamma}$, which forms the basis of the deformation potential γ_i, is a quantity derived from the elastic tensor $\bar{\epsilon}$, as

$$\bar{\gamma} = \frac{\delta\Delta}{\delta\bar{\epsilon}}. \tag{5}$$

Formally, γ_i can be defined in the transverse and the longitudinal directions, according to the direction of the strain. In a disordered system, TLSs are isotropic; as such, we average γ_i over all strain directions,

$$\begin{aligned}\gamma_L^2 = {} & \tfrac{1}{5}\left(\bar{\gamma}_{XX}^2 + \bar{\gamma}_{YY}^2 + \bar{\gamma}_{ZZ}^2\right) \\ & + \tfrac{2}{15}\left(\bar{\gamma}_{XX}\bar{\gamma}_{YY} + \bar{\gamma}_{XX}\bar{\gamma}_{ZZ} + \bar{\gamma}_{YY}\bar{\gamma}_{ZZ}\right) \\ & + \tfrac{4}{15}\left(\bar{\gamma}_{XY}^2 + \bar{\gamma}_{XZ}^2 + \bar{\gamma}_{YZ}^2\right),\end{aligned} \tag{6}$$

for the longitudinal modulus, and

$$\begin{aligned}\gamma_T^2 = {} & \tfrac{1}{15}\left(\gamma_{XX}^2 + \gamma_{YY}^2 + \gamma_{ZZ}^2\right) \\ & - \tfrac{1}{15}\left(\gamma_{XX}\gamma_{YY} + \gamma_{YY}\gamma_{ZZ} + \gamma_{ZZ}\gamma_{XX}\right) \\ & + \tfrac{3}{15}\left(\gamma_{YY}^2 + \gamma_{YZ}^2 + \gamma_{YZ}^2\right),\end{aligned} \tag{7}$$

for the transverse modulus. The detailed derivation for the equations above can be found in Ref. [23]. Not all TLSs contribute to noise in the frequency range where GWD detection

is affected by this noise. In Ref. [16], the barrier range of the contributing TLSs was identified to be between 0.2 and 0.7 eV.

B. Moment-tensor potential

Recent work on TLSs in amorphous materials was mostly pursued using an empirical potential, whether the van Beest–Kramer–van Santen potential (BKS) [24] for silica [23], a combination of BKS and Morse potential in TiO_2:Ta_2O_5 [8] or a mSW potential [15,25] for *a*-Si [16].

However, it has been shown that barriers generated with these potentials might not correspond to saddle points obtained with a more precise DFT representation [18]. As it is not possible to broadly explore with DFT the energy landscape of amorphous systems, we select to use a DFT-based machine-learned potential recently developed for *a*-Si by Zongo *et al.* [21].

This force field was created using the moment-tensor potential (MTP) description [20] and adjusted to the DFT energies and forces for a wide range of silicon structures, including the amorphous phase. The theory behind constructing MTP is based on the assumption that it is possible to approximate any potential through a complex series of polynomials.

A more in-depth explanation of MTP and the construction of the polynomial is given in Ref. [20]. The parameters used here were developed as part of an effort to construct a universal potential for both Si and SiO_2 following a training schedule presented in Ref. [21]. While the general validity of the potential is presented in that work, a more specific characterization of the potential's quality for *a*-Si can be found in Ref. [26]. This paper shows that the potential favors low-defect structures with overall properties in excellent agreement with experiments and other high-quality modeling results.

C. Atomic models

To facilitate the comparison with previously published results, we closely follow the melt-and-quench schedule used in Ref. [16] to generate unbiased and independent high-quality 1000-atom *a*-Si models.

Each model is created starting with a 1000-atom crystalline cell that is heated at 3000 K for 1 ns with a randomly generated initial velocity distribution. The configuration is then brought to 1500 K at a relatively high rate of 1.5×10^{13} K/s and then cooled to 300 K at a much slower rate of 1.0×10^{11} K/s. After a 1 ns equilibration at 300 K, to eliminate the low-energy barriers, the configuration is minimized at 0 K at constant pressure of $P = 0$ Pa. As the computation cost of MTP is about 100 times higher than for the mSW potential due to the high complexity of the local descriptors and the larger number of parameters evaluated as compared with standard empirical potentials, we limit the number of independent samples to 28 instead of the 200 produced with mSW [16]. As seen below, since the density for TLSs in the MTP-based models is higher than for mSW models, the quality of statistics remains sufficient to draw meaningful conclusions.

D. ART nouveau

To identify the TLSs present in the system, it is necessary to extensively explore the energy landscape surrounding each final configuration. To do so, we use the activation-relaxation technique nouveau (ARTn) [27–30], an efficient open-ended transition-state searching method. Here, each event search is centered on a specific atom. Starting from a local minimum, an initial random deformation is applied on a central atom and its first neighbors (within a radius of 2.9 Å). The system is deformed slowly along this direction, with slight perpendicular relaxation at each step to avoid collision, until the lowest eigenvalue of the Hessian matrix becomes negative (below a threshold of −1 eV/Å), indicating that a direction of instability has been found. The system is then pushed away from the minimum along this direction of negative curvature, with forces minimized in the hyperplane perpendicular to this direction until the total force falls below 0.01 eV/Å, indicating that a saddle point has been reached. The system is then minimized after being slightly displaced from the saddle point in both directions along the eigenvector corresponding to the negative eigenvalue to find the final state and ensure that the saddle point is connected to the initial state. If this is the case, the event is added to the catalog. Events are classified according to the automorphic group associated with the graph formed by the bonding network of the atoms found in a radius of 6.5 Å around the central atom. As discussed in Ref. [29], this graph provides a reliable framework for classifying events.

To generate the full event catalog, we launched 30 event searches centered on each atom in the cell, for a total of 30 000 event searches per configuration, leading to a total of 52 000 topologically different events with a barrier below 5 eV for the 28 configurations. Only events corresponding to the TLS criteria are discussed below. As the first event classification done using the local topology can overcount the number of different events, the list of TLSs is further refined with geometrical criteria based on relative displacements to remove the rare cases of overcounting, when the same structure is linked with two different topologies due to small deformations associated with a soft environment.

III. RESULTS

The quality of the resulting configurations is assessed by comparing the structural properties of the MTP-generated samples to available experimental data and samples generated through melt and quench using the mSW potential. Events generated are described by a barrier height, the energy asymmetry, and the energy of the original and final minima and of the saddle point. We use the criteria retained in Sec. II A and described above to identify the TLSs that contribute to the internal friction (loss angle) in GWD experiments. The properties of these events are also compared to previous results obtained on samples generated with mSW [16].

A. Prefactor analysis

Recent work has shown that activated prefactors,τ_0 in Eq. (2), can vary widely in disordered materials [31]. It is therefore necessary to assess whether it is possible to use the general approximation of a constant prefactor for the TLSs considered here.

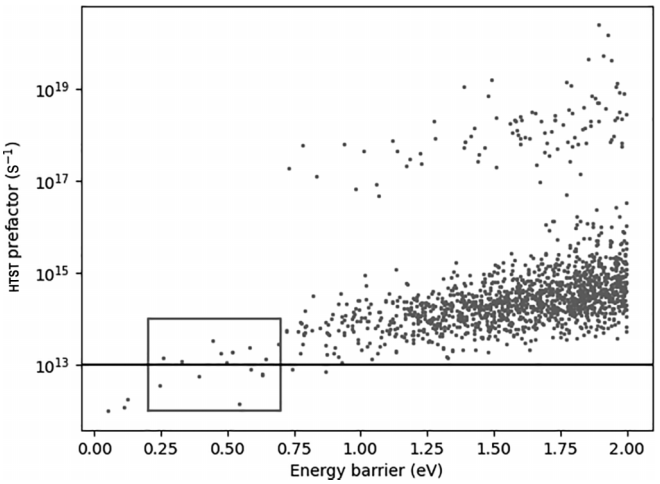

FIG. 2. Attempt frequency, or prefactor, given by the harmonic transition theory, as a function of energy barrier for all events with a barrier below 5 eV found in a representative 1000-atom *a*-Si configuration prepared as discussed in the text. The green rectangle indicates the data range studied in the present work and the black line indicates the constant prefactor usually used for *a*-Si.

To do so, we use the harmonic approximation of the transition-state theory (HTST),

$$\tau_{\mathrm{HTST}}^{-1} = \frac{\prod_{i=1}^{3N} \nu_i}{\prod_{j=1}^{3N-1} \nu'_j}, \tag{8}$$

where ν_i are the real eigenfrequencies of the Hessian matrix.

Because of the computational cost associated with this calculation, we assess the evolution of the prefactor for all 1563 events with a barrier below 5 eV found in a single representative configuration. Figure 2 presents the prefactor of each cataloged event as a function of the associated energy barrier of the associated event for this configuration. The green rectangle indicates the region that includes TLSs. While the distribution of rates is broad for events with energy barriers above 1.0 eV, and further analysis is required to understand the nature of the very high prefactors observed in this region, we see that for energy barriers between 0.2 and 0.7 eV, the prefactor is found to be $(1.4 \pm 0.9) \times 10^{13}$ Hz, compatible with the typical constant rate of 1×10^{13} used previously for computing activation rates [16,23]. It is therefore appropriate to follow the convention and use a constant $\tau_0 = 1 \times 10^{-13}$ s in the energy regime that is relevant here.

B. Quality of models

Table I presents the average structural and energetic properties with the standard deviation computed over the 28 samples prepared following the procedure described in Sec. II C. The quality of these models is established by comparing with similar *a*-Si models generated following the same cooling schedule, but using the mSW potential [16] as well as experimental results, when available.

The final configurations for MTP-generated models show an energy per atom that is 0.14 eV above that of the crystalline configuration at optimal density, as compared with the 0.135–0.205 eV/atom from experiments [32] and 0.22 eV/atom obtained with the mSW. At 2.23 g/cm^3, the density for MTP samples is slightly lower than the experimental value (2.28 g/cm^3) and similar to that produced with the mSW (2.2 g/cm^3). Regarding defects, the MTP samples contain $1.6 \pm 0.6\%$ overcoordinated atoms (fivefold coordinated) and $0.6 \pm 0.2\%$ undercoordinated defects (threefold coordinated), a value similar to that observed in mSW samples, with $1.7 \pm 0.4\%$ overcoordinated and $0.7 \pm 2\%$ undercoordinated atoms.

In Fig. 3 (top panel), we also compare the radial distribution for both MTP- and mSW-generated samples with experimental data obtained using *a*-Si membranes prepared by self-implantation [33]. We observe good agreement between the various models and experiment, although, because models are evaluated at $T = 0$ K, the first peak, associated with the nearest neighbors, is narrower than for the experimental system, which shows a thermal broadening. While experimental data are not available for the angular distribution, we see in the lower panel of Fig. 3 that both sets of models provide a similar distribution.

Overall, the structural properties of the MTP-based models produced through a melt-and-quench procedure are very similar to available mSW-generated results and comparable to experiments. Nevertheless, even considering the dispersion

TABLE I. Properties of *a*-Si prepared by melt and quench with MTP (this article) and with mSW [16]. This includes the configurational energy E_c and the strain energy with respect to the crystal (E_{strain}) per atom; the density ρ, the number of overcoordinated, fivefold, and undercoordinated, threefold, atoms per 1000 atoms; the number of TLSs in total and per 1000 atoms; and the number of independent configurations (N_{samples}). The properties are averaged for a sample size of 200 for mSW and 28 for MTP with uncertainty corresponding to the standard deviation. Experimental density is taken from Ref. [34] and experimental energy difference betwen crystalline and amorphous configuration from Ref. [32].

Sample	mSW	MTP	Experimental
E_c (eV/at.)	-3.078 ± 0.004	-635.604 ± 0.002	
E_{strain} (eV/at.)	0.219 ± 0.004	0.140 ± 0.002	0.135–0.205 [32]
ρ (g/cm^3)	2.200 ± 0.006	2.231 ± 0.001	2.280 [34]
Fivefold/1000 at.	17 ± 4	16 ± 6	
Threefold/1000 at.	7 ± 2	6 ± 2	
TLSs (total)	390	117	
TLSs/1000 at.	1.95	4.18	
N_{samples}	200	28	

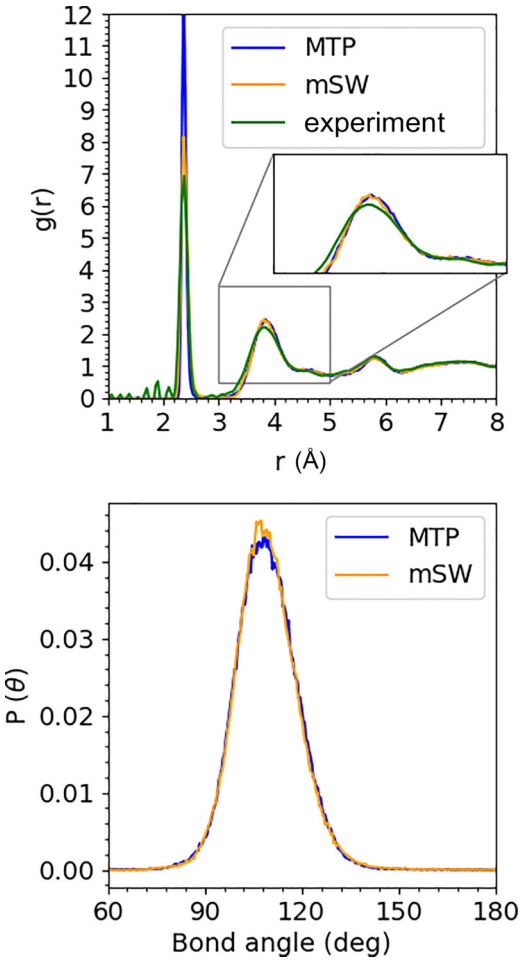

FIG. 3. Top panel: The mean radial distribution function (RDF) for the MTP (total of 28 samples), the mSW (total of 200 samples) models, and from diffraction experiments (EXPT) [33]. Bottom panel: The mean angular distribution function for the two sets of models.

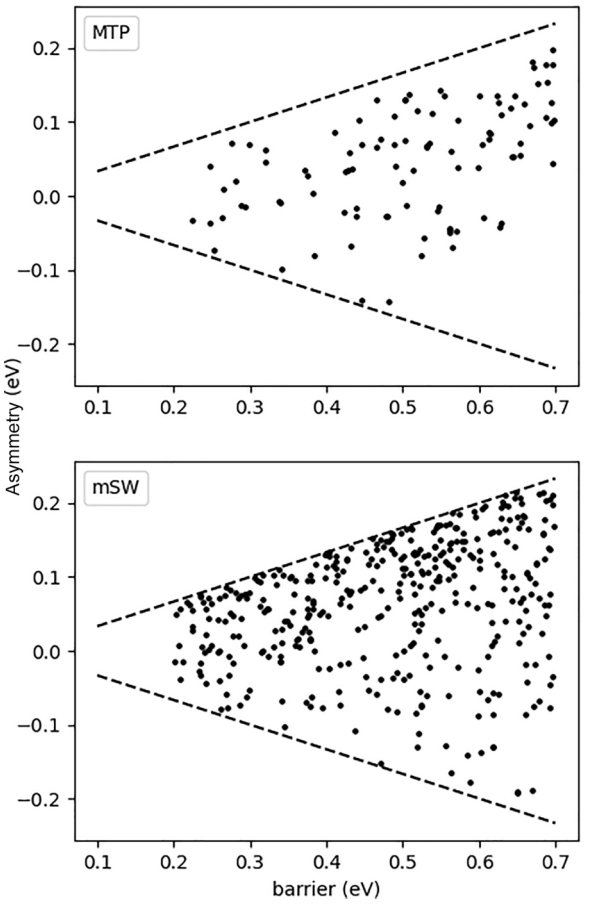

FIG. 4. Energy asymmetry as a function of the forward-energy barrier for events corresponding to the TLS definition criteria. The dotted lines delimit the cone of the acceptable asymmetry as a function of energy barrier. Top panel: results generated in this study. Bottom panel: TLSs generated using mSW and taken from Ref. [16].

in the data, an argument can be made, taking into account all results presented in Table I, that MTP-based structures are less strained, show a similar number of defects, and are in overall slightly closer agreement with experiments than mSW-based models generated with the same simulation schedule using a potential specifically fitted to this phase of silicon. However, the difference for these structural properties is narrow and no differences in structural properties stand out between the two potentials.

C. Two-level systems

We now turn to the characterization of the energy landscape, focusing on the TLSs. Out of the 52 000 events present in the catalog described in Sec. II D, we identify 117 unique TLSs (4.18 TLSs per 1000 atoms) that respect the required conditions on energy and asymmetry: a barrier V, between 0.2 and 0.7 eV, which is at the origin of noise at a frequency around 50 Hz for temperatures between 124 and 300 K, the temperature at which the mirrors of GWD are kept. The energy asymmetry between the two connected minima, Θ, such that $\Theta \leqslant V/3$ [23], is classified as a TLS, as illustrated in Fig. 4. As indicated in Table I, the number of TLSs found here corresponds to a TLS density that is more than double that found with samples prepared using mSW (1.95 TLS/1000 atoms). (It is worth noting that despite a higher TLS density with the MTP, smaller TLSs statistics appear in the top panel of Fig. 4 because 28 samples were studied, compared to 200 with the mSW potential.)

Figure 4 (top panel) shows the energy asymmetry as a function of the energy barrier for the 117 TLSs measured from the initial state. Because each initial state is the end result of the extended quenching schedule presented above, we observe an asymmetry in the energy of the second states of TLSs, which are more often of higher energy, in agreement with previous observations [35]. This does not prevent, of course, some final states from having a lower energy than their initial counterpart, especially in the case of lower (less than 0.5 eV) forward-energy barriers, as measured from the initial state of the simulation.

The energy distribution of TLSs is very similar to that obtained using mSW [16] (bottom panel of Fig. 4). The mean barrier energy of the MTP samples is 0.51 ± 0.13 eV, compared to 0.48 ± 0.14 eV for the mSW samples.

Figure 5 shows the root-mean-square displacement of the atoms as a function of the barrier energy. The number of atoms

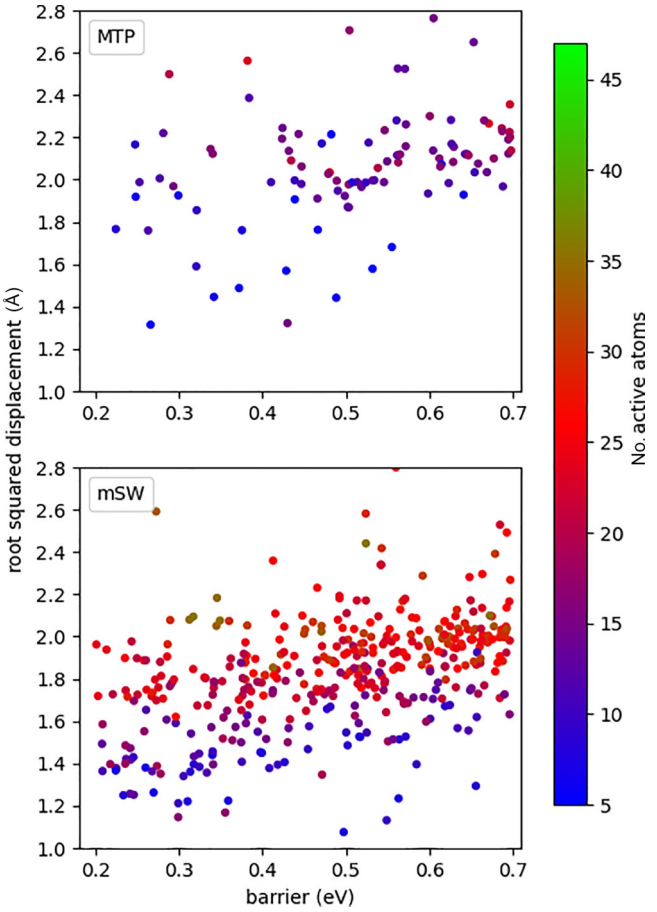

FIG. 5. Mean-square displacement between the initial and final states of TLSs as a function of the forward-energy barrier. Symbols are colored according to the number of atoms moving by more than 0.1 Å between the two states. Top panel: results generated in this study. Bottom panel: TLS generated using mSW and taken from Ref. [16].

displaced by more than 0.1 Å between their initial and final states for each TLS is indicated by a color gradient. Again, the top panel shows the results for the samples obtained with the MTP, while the bottom panel is for the TLSs previously found with the mSW potential. Although the average distance between minima is 2.05 ± 0.25 Å for TLSs generated in MTP samples, slightly longer than the 1.81 ± 0.27 Å for mSW, MTP TLSs tend to involve fewer atoms (14 ± 4 vs 22 ± 7 considering a range of one standard deviation). This suggests that the MTP energy landscape is somewhat smoother than mSW's: most atoms disturbed during activation therefore recover their original position, while those that move often need to make a bigger displacement to find a new stable position.

Finally, we present the histogram of the density of TLSs per 1000 atoms as a function of the forward-energy barrier height, comparing MTP and mSW results (Fig. 6). As indicated in the previous section, the overall density of MTP-based TLSs is higher than that for mSW models. The difference is not uniform, however: while the distribution is relatively flat for mSW samples, MTP-based TLSs of energy higher than 0.4 eV are clearly more frequent. This bias toward higher forward-energy barriers can be explained by the lower

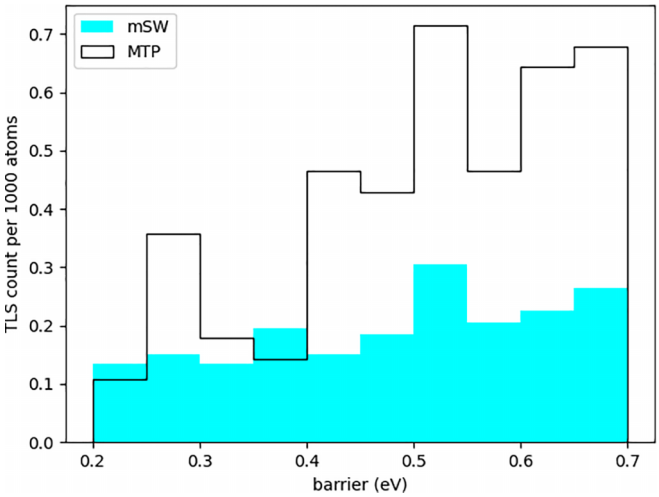

FIG. 6. Histogram of the density of TLS events per 1000 atoms as a function of the forward-energy barrier for MTP and mSW [16] results.

strain of the MTP models: with less energy stored in deformation, higher barriers need to be crossed to change state. Moreover, the more rigid network, observed when looking at the number of atoms involved in each event, might signify that local relaxation requires breaking bonds and that it cannot be accomplished simply with a slight diffusivelike shift of atoms.

D. Categorization of the TLSs

Following Ref. [16], we categorize the TLSs according to the nature of the connectivity changes between the two linked minima: the first category of events represents bond-hop events, where one atom reduces its coordination to the benefit of a first-neighbor atom. The second category defines events that involve a Wooten-Winer-Weaire (WWW) bond-exchange mechanism [36], a common occurrence in *a*-Si [37,38]; this type of event involves two connected atoms exchanging a neighbor, while maintaining coordination for all atoms involved. We place all events that do not belong to either of these categories in a third class. To limit the effects of the cutoff, only atoms that move by at least 1 Å are considered for the definition of a bond hop or a bond-exchange event.

Among the 117 TLSs found, 19% are bond-hopping events, 40% are bond-exchange events, and 41% are in the other category. In Fig. 7, the density of TLSs per 1000 atoms for each type of TLS for both mSW- and MTP-generated samples is illustrated. For bond-hopping events, a similar density of events is recorded, while there is a disparity between the models for both the bond-exchange events and the uncategorized events. As such, the difference in proportion of bond-hopping events compared to the other categories is only due to the higher number of bond-exchange events and uncategorized events. The contributions of the different types of TLSs to the density depending on barrier height are better illustrated in Fig. 8. In the top figure, the density of occurrences of each species is illustrated for the MTP-generated samples. Lower barrier contributions to the density (below 0.5 eV) are mainly from bond-hopping and uncategorized events, with contributions to higher-energy barrier events

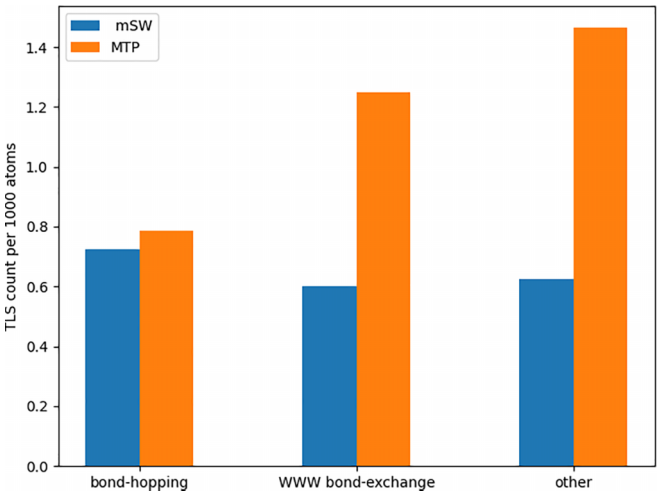

FIG. 7. Average number of TLSs per 1000 atoms that belong to each of the three bond switching categories for the MTP-based (orange bars) and mSW-based (blue bars) models.

originating mainly from bond-exchange events. Overall, while the relatively small number of events leads to high fluctuations, bond-hopping events are concentrated in the low-energy barrier fraction of TLs, bond-exchange events, in the high-energy fraction, while the other category is distributed across the range. In the bottom panel of Fig. 8, a similar histogram is illustrated, but only encompassing results from mSW-generated samples. The difference in TLS density is smallest for the bond-hopping events, as can be seen when comparing the data for the two types of samples at 0.038 ± 0.019 with that of the "other" events at 0.1 ± 0.0 and the bond-exchange events at 0.1 ± 0.2. At higher energy, the contribution of bond-exchange events to the density is notably larger than what was estimated with the mSW potential, which is consistent with the previous observation that bond-exchange events are much more common with MTP than with mSW.

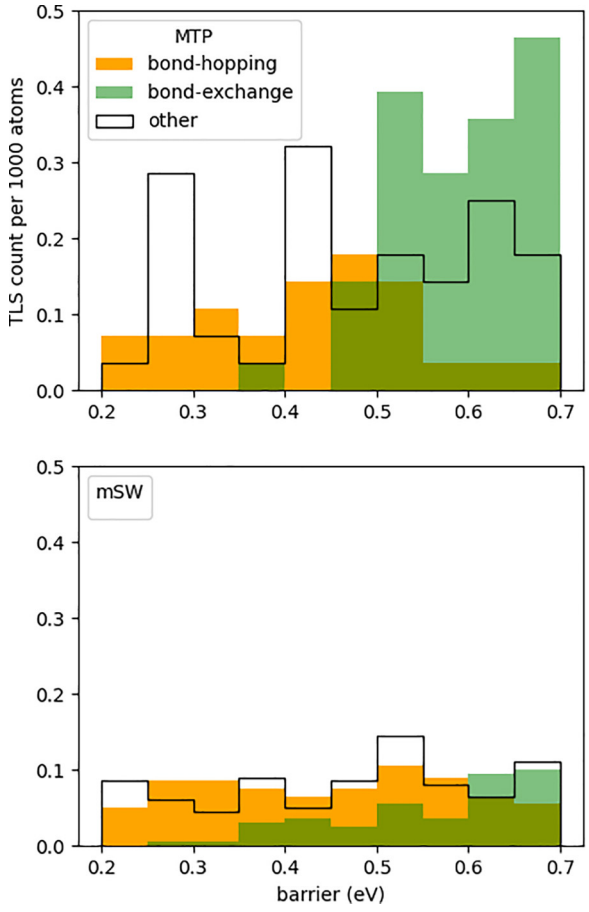

FIG. 8. Density of TLS species per 1000 atoms in term of energy barrier for MTP (top) and mSW (bottom) [16].

E. Correlations between events

Recent works have suggested that amorphous materials could display a much higher density of connected TLSs that would lead to the same experimental signature as rare isolated TLSs [39]. To assess whether this suggestion applies here, we examine whether the TLSs we generated are connected.

While ARTn generated pure TLSs, composed of two minima directly connected by a common first-order saddle point, TLSs could be linked between themselves, forming a larger dissipative basin composed of multiple minima that would effectively decrease the number of independent TLSs [39]. To assess the proportion of these larger basins, we count the number of events with overlapping participating atoms, i.e., atoms in the same sample that move by at least 1 Å.

We find that most TLSs recorded (99 events) in most samples (22 out of 28) are unique events, involving atoms that do not participate in other events. Of the total 117 TLSs found, 15% of these, concentrated in six samples, are identified as involving active atoms recurring in different events: five pairs of events are part of basins containing two events and two sets of four-overlapping-event basins; the 99 other events are not connected to any other events and are isolated in their respective basin.

The weak spatial correlation between TLSs is coherent with events which are local in nature, including single bond hop and bond exchanges, and that can be analyzed with the theory presented in Sec. II A and applied next.

F. Loss-angle calculation

Using Eq. (3), we compute the loss angle Q^{-1} as a function of temperature by summing the contribution of each TLS generated with the MTP. We compare that sum with measurements of the mechanical dissipation in *a*-Si from two samples of *a*-Si grown by electron-beam evaporation at 45 °C and 200 °C [11] as well as the sum obtained from the simulations with the mSW potential. The latter is computed again for the current study as a factor 4 had been omitted in the calculation of the elastic modulus in Ref. [16]; this leads to an overall downward shift of the curve with respect to the one presented in that reference.

As illustrated in Fig. 9, the noise computed from MTP data shows an excellent overlap with experimental results, suggesting that both the density and the distribution of TLSs computed with that potential are closer to what is observed experimentally than those computed using an mSW potential.

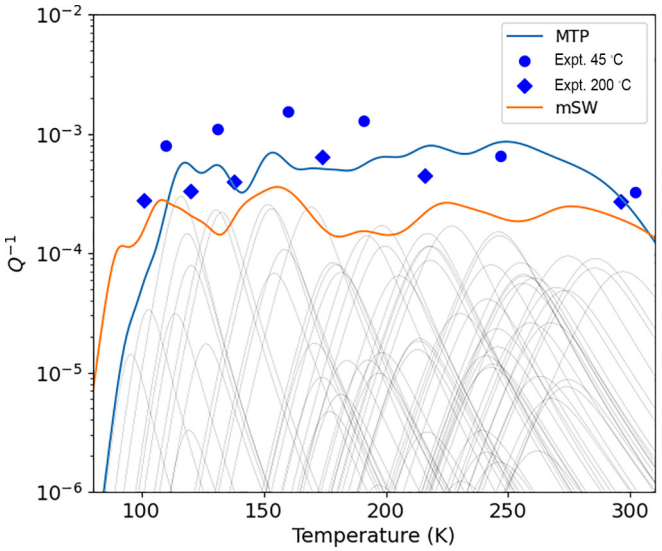

FIG. 9. Loss-angle contribution for MTP, mSW (recomputed with respect to Ref. [16]), and experimental results [11]. In gray, the contribution of individual TLSs of the MTP catalog to the mechanical noise.

G. Validation of the MPT events

To estimate the validity of the saddle points discussed above, TLS minima and saddle points obtained with MPT are reconverged using the mSW potential, as well as two MPT potentials with different levels of description fitted to the same Gaussian approximation potential (GAP), a DFT-based general-purpose ML potential for Si [40], by Morrow *et al.* [41]. More specifically, we consider here the indirect 16 (Ind16) and indirect 20 (Ind20) potentials of Ref. [41]. This comparison with two potentials fitted to the same high-quality dataset allows for a better estimation of the intrinsic value of the results.

Figure 10 shows the displacement from the various minima obtained with MTP when reminimized with the three potentials. While Ind16 and Ind20 show a displacement of around 1 Å away from the initial minima for the 1000-atom configurations, the mSW leads to significantly larger relaxations away

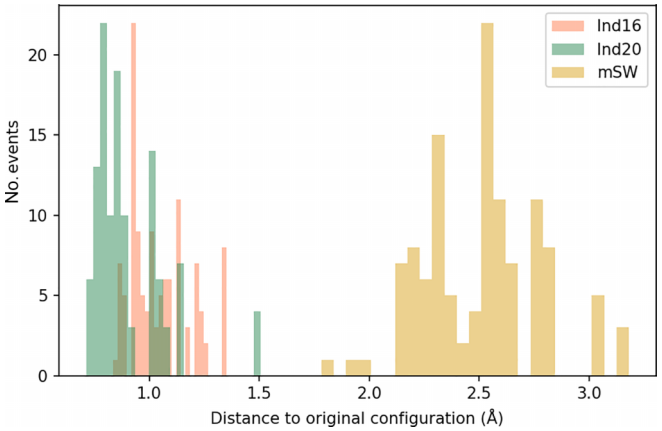

FIG. 10. Displacement from minimum-energy configuration generated with MPT after relaxation with the empirical aSW as well as two ML potentials: Ind16 and Ind20.

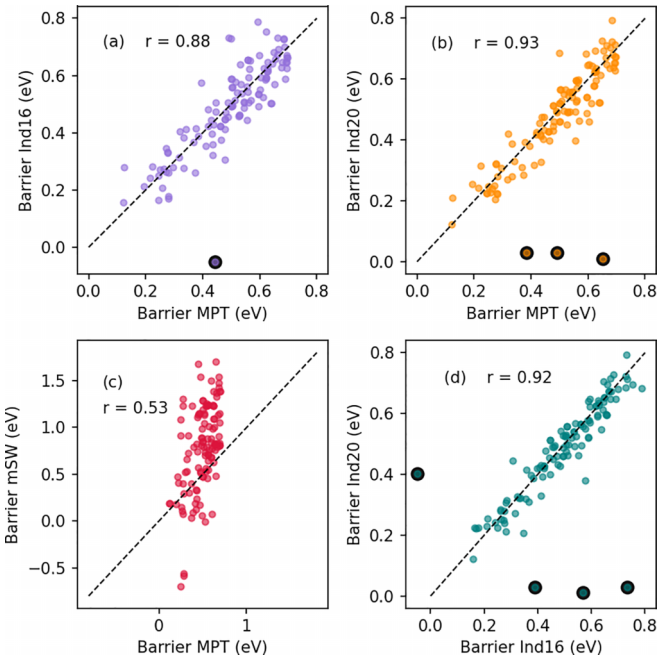

FIG. 11. Correlations between the barrier height for MPT-generated TSL saddle points and the saddle points found after a further convergence with (a) Ind16, (b) Ind20, and (c) aSW potentials. (d) Correlations between the barrier heights obtained with Ind16 and Ind20. R-values indicated in the panel show the regression coefficient. Points surrounded by a black line are not included in the evaluation of the regression coefficient.

from the MPT minima, suggesting that MPT minima are not stable with mSW.

To assess the quality of saddle points, we plot the correlations for the saddle energy (Fig. 11) and the displacement from the initial minimum to the saddle point (Fig. 12) between the MPT structures, discussed previously, and those obtained after further convergence with Ind16, Ind20, and mSW. Looking at Fig. 11, we note that the majority of the saddle points is reconverged to structures that are energetically close to the initial MTP structure, except for a handful of saddle points (one for Ind16 and a different set of three for Ind20) that relax into a minimum-energy state (barrier near zero eV). If we set aside these few points, we find a similar degree of correlation between the three ML potentials, with a slightly better agreement between Ind20 and MPT, even though Ind16 and Ind20 are fitted to the same data set. As expected from the comparisons made in the previous sections, the correlation is much lower when compared with mSW. Results are similar when we compare the displacement between the initial minimum and the saddle point, confirming the strong similarity in the structures converged by the three ML potentials and, in particular, between MPT and the richer Ind20, even though very few barriers are not reproduced by the three potentials.

IV. CONCLUSIONS

Twenty-eight samples of *a*-Si were prepared by melt and quench using a recently developed DFT-based machine-learned moment-tensor potential (MTP) [21]. The energy

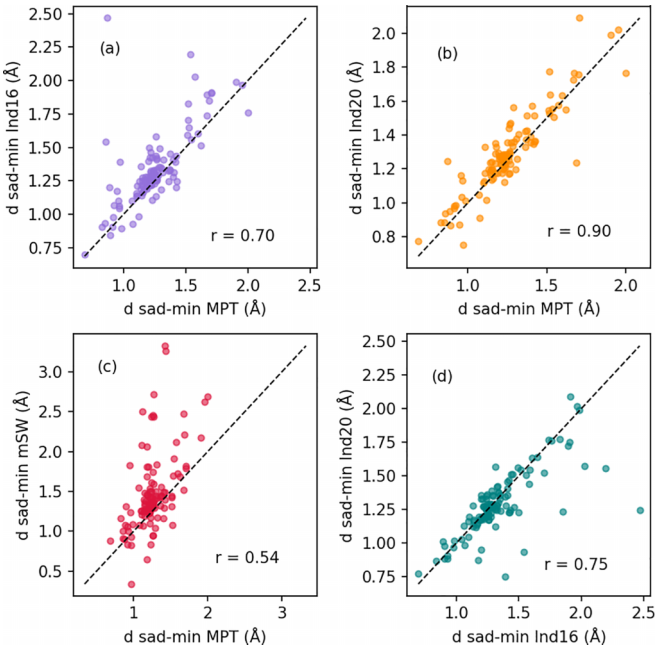

FIG. 12. Correlations between the displacement between the saddle point and initial minimum for MPT-generated TSL saddle points; the displacement is found after a further convergence with (a) Ind16, (b) Ind20, and (c) aSW potentials. (d) Correlations between the barrier heights obtained with Ind16 and Ind20. R-values indicated in the panel show the regression coefficient. Points surrounded by a black line in Fig. 11 are not plotted nor included in the evaluation of the regression coefficient.

landscape of these samples was explored using ARTn to identify TLSs. Out of 52 000 different generated events, 117 were found to correspond to TLSs that contribute to the mechanical dissipation mechanisms in the frequency and temperature range relevant to reproduce the noise observed in GWD.

The properties of the samples and of the TLSs were then compared with samples generated in a similar fashion but using the empirical mSW potential [16], to measure and validate the importance of using DFT-based potentials in the study of activated mechanisms. The use of MTP leads to amorphous models with slightly fewer defects than those generated with mSW, with a marginally better agreement on these structural properties compared to experiments. This is expected since mSW was modified to address some of the shortcomings of the SW potential in generating realistic models of *a*-Si [15]. Differences are more important when looking at the energy landscape. In spite of similar defect concentration, MTP models show a TLS density twice that of mSW, with a dominance of compact complex events, while mSW favors simple bond-hopping mechanisms, with longer-range deformation. These changes are captured, at the macroscopic level, in the loss-angle contribution, with MTP presenting a better agreement with experiments than mSW.

While generally producing the right picture, these results underline the limits of empirical potentials for the specific description of atomistic mechanisms in disordered systems, even when they lead to reasonable average properties. Of course, there can still be variations between ML-fitted potentials; they can be significantly smaller than those between these and empirical potentials, when fitted to sufficiently large datasets, as shown here. Further methodological improvment remains necessary, however, to improve the reproduction of barriers even with ML potentials [42].

Getting the atomistic details right is essential to really understand phenomena such as dissipation caused by TLSs and develop efficient strategies to reduce it. With higher confidence in the modeling results regarding the structure and kinetics of amorphous silicon, future work will be able to provide more reliable answers to these specific questions.

ACKNOWLEDGMENTS

This research was supported in part by the NSERC Discovery program and generous computing time allocation provided by Calcul Québec and the Digital Research Alliance of Canada. The authors would like to thank Sjoerd Roorda and members of the LIGO Scientific Collaboration's Optics Working Group for useful discussions.

DATA AVAILABILITY

The data that support the findings of this article are openly available [43], embargo periods may apply.

[1] A. G. Abac *et al.* (The LIGO Scientific Collaboration, The Virgo Collaboration, and The KAGRA Collaboration), GWTC-4.0: An introduction to version 4.0 of the gravitational-wave transient catalog, Astroph. J. Lett. **995**, L18 (2025).

[2] S. Clesse and J. García-Bellido, The clustering of massive primordial black holes as dark matter: Measuring their mass distribution with advanced LIGO, Phys. Dark Universe **15**, 142 (2017).

[3] B. Abbott, R. Abbott, T. Abbott, M. Abernathy, F. Acernese, K. Ackley, C. Adams, T. Adams, P. Addesso, R. X. Adhikari, V. B. Adya, and C. Affeldt, GW150914: The Advanced LIGO detectors in the era of first discoveries, Phys. Rev. Lett. **116**, 131103 (2016).

[4] R. Nawrodt, S. Rowan, J. Hough, M. Punturo, F. Ricci, and J.-Y. Vinet, Challenges in thermal noise for 3rd generation of gravitational wave detectors, Gen. Relativ. Gravit. **43**, 593 (2011).

[5] S. J. Waldman, The Advanced LIGO gravitational wave detector, arXiv:1103.2728.

[6] R. Kubo, The fluctuation-dissipation theorem, Rep. Prog. Phys. **29**, 255 (1966).

[7] W. A. Phillips, Two-level states in glasses, Rep. Prog. Phys. **50**, 1657 (1987).

[8] J. P. Trinastic, R. Hamdan, C. Billman, and H.-P. Cheng, Molecular dynamics modeling of mechanical loss in amorphous tantala and titania-doped tantala, Phys. Rev. B **93**, 014105 (2016).

[9] K. Prasai, K. Lee, B. Baloukas, H.-P. Cheng, M. Fazio, L. Martinu, A. Mehta, C. S. Menoni, F. Schiettekatte, R. Shink, B. Shyam, G. Vajente, M. M. Fejer, and R. Bassiri, Effects of elevated-temperature deposition on the atomic structure of amorphous Ta_2O_5 films, APL Mater. **11**, 121112 (2023).

[10] G. M. Harry, A. M. Gretarsson, P. R. Saulson, S. E. Kittelberger, S. D. Penn, W. J. Startin, S. Rowan, M. M. Fejer, D. R. M. Crooks, G. Cagnoli, J. Hough, and N. Nakagawa, Thermal noise in interferometric gravitational wave detectors due to dielectric optical coatings, Classic. Quantum Gravit. **19**, 897 (2002).

[11] X. Liu, D. R. Queen, T. H. Metcalf, J. E. Karel, and F. Hellman, Hydrogen-free amorphous silicon with no tunneling states, Phys. Rev. Lett. **113**, 025503 (2014).

[12] J. Steinlechner, I. W. Martin, J. Hough, C. Krüger, S. Rowan, and R. Schnabel, Thermal noise reduction and absorption optimization via multimaterial coatings, Phys. Rev. D **91**, 042001 (2015).

[13] M. Molina-Ruiz, R. Zhou, A. Markosyan, R. Bassiri, M. M. Fejer, A. Ananyeva, S. C. Tait, G. Vajente, A. Davenport, C. S. Menoni, and F. Hellman, Revealing the role of hydrogen in reducing optical absorption and mechanical loss in magnetron-sputtered amorphous silicon for gravitational-wave detectors, Phys. Rev. Mater. **9**, 105602 (2025).

[14] E. Lalande, J. Vanier, A. W. Lussier, L. Martinu, J. Steinlechner, A. Amnache, S. Ecoffey, and F. Schiettekatte, Crystalline/amorphous silicon and silica Bragg reflectors for gravitational wave detectors (unpublished).

[15] R. Vink, G. Barkema, W. Van Der Weg, and N. Mousseau, Fitting the Stillinger-Weber potential to amorphous silicon, J. Non-Cryst. Solids **282**, 248 (2001).

[16] C. Lévesque, S. Roorda, F. Schiettekatte, and N. Mousseau, Internal mechanical dissipation mechanisms in amorphous silicon, Phys. Rev. Mater. **6**, 123604 (2022).

[17] R. Birney, J. Steinlechner, Z. Tornasi, S. MacFoy, D. Vine, A. S. Bell, D. Gibson, J. Hough, S. Rowan, P. Sortais, S. Sproules, S. Tait, I. W. Martin, and S. Reid, Amorphous silicon with extremely low absorption: Beating thermal noise in gravitational astronomy, Phys. Rev. Lett. **121**, 191101 (2018).

[18] A. Jay, A. Hemeryck, N. Richard, L. Martin-Samos, M. Raine, A. Le Roch, N. Mousseau, V. Goiffon, P. Paillet, M. Gaillardin, and P. Magnan, Simulation of single-particle displacement damage in silicon—Part III: First principle characterization of defect properties, IEEE Trans. Nucl. Sci. **65**, 724 (2018).

[19] I. S. Novikov and A. V. Shapeev, Improving accuracy of interatomic potentials: More physics or more data? A case study of silica, Mater. Today Commun. **18**, 74 (2019).

[20] A. V. Shapeev, Moment tensor potentials: A class of systematically improvable interatomic potentials, Multiscale Model. Simulat. **14**, 1153, (2016).

[21] K. Zongo, H. Sun, C. Ouellet-Plamondon, and L. K. Béland, A unified moment tensor potential for silicon, oxygen, and silica, npj Comput. Mater. **10**, 218 (2024).

[22] D. G. Truhlar, B. C. Garrett, and S. J. Klippenstein, Current status of transition-state theory, J. Phys. Chem. **100**, 12771 (1996).

[23] T. Damart and D. Rodney, Atomistic study of two-level systems in amorphous silica, Phys. Rev. B **97**, 014201 (2018).

[24] B. W. H. van Beest, G. J. Kramer, and R. A. van Santen, Force fields for silicas and aluminophosphates based on *ab initio* calculations, Phys. Rev. Lett. **64**, 1955 (1990).

[25] F. H. Stillinger, Role of potential-energy scaling in the low-temperature relaxation behavior of amorphous materials, Phys. Rev. B **32**, 3134 (1985).

[26] K. Zongo, H. Sun, C. Ouellet-Plamondon, N. Mousseau, and L. K. Béland, Amorphous silicon structures generated using a moment tensor potential and the activation relaxation technique nouveau, Phys. Rev. B **111**, 214209 (2025).

[27] G. T. Barkema and N. Mousseau, Event-based relaxation of continuous disordered systems, Phys. Rev. Lett. **77**, 4358 (1996).

[28] R. Malek and N. Mousseau, Dynamics of Lennard-Jones clusters: A characterization of the activation-relaxation technique, Phys. Rev. E **62**, 7723 (2000).

[29] N. Mousseau, L. K. Béland, P. Brommer, J.-F. Joly, F. El-Mellouhi, E. Machado-Charry, M.-C. Marinica, and P. Pochet, The activation-relaxation technique: ART nouveau and kinetic ART, J. Atom. Molec. Opt. Phys. **2012**, 1 (2012).

[30] A. Jay, C. Huet, N. Salles, M. Gunde, L. Martin-Samos, N. Richard, G. Landa, V. Goiffon, S. De Gironcoli, A. Hémeryck, and N. Mousseau, Finding reaction pathways and transition states: r-ARTn and d-ARTn as an efficient and versatile alternative to string approaches, J. Chem. Theory Comput. **16**, 6726 (2020).

[31] S. Gelin, A. Champagne-Ruel, and N. Mousseau, Enthalpy-entropy compensation of atomic diffusion originates from softening of low frequency phonons, Nat. Commun. **11**, 3977 (2020).

[32] D. K. Limbu, R. Atta-Fynn, D. A. Drabold, S. R. Elliott, and P. Biswas, Information-driven inverse approach to disordered solids: Applications to amorphous silicon, Phys. Rev. Mater. **2**, 115602 (2018).

[33] K. Laaziri, S. Kycia, S. Roorda, M. Chicoine, J. L. Robertson, J. Wang, and S. C. Moss, High resolution radial distribution function of pure amorphous silicon, Phys. Rev. Lett. **82**, 3460 (1999).

[34] J. S. Custer, M. O. Thompson, D. C. Jacobson, J. M. Poate, S. Roorda, W. C. Sinke, and F. Spaepen, Density of amorphous Si, Appl. Phys. Lett. **64**, 437 (1994).

[35] H. Kallel, N. Mousseau, and F. Schiettekatte, Evolution of the potential-energy surface of amorphous silicon, Phys. Rev. Lett. **105**, 045503 (2010).

[36] F. Wooten, K. Winer, and D. Weaire, Computer generation of structural models of amorphous Si and Ge, Phys. Rev. Lett. **54**, 1392 (1985).

[37] G. T. Barkema and N. Mousseau, Identification of relaxation and diffusion mechanisms in amorphous silicon, Phys. Rev. Lett. **81**, 1865 (1998).

[38] F. Valiquette and N. Mousseau, Energy landscape of relaxed amorphous silicon, Phys. Rev. B **68**, 125209 (2003).

[39] S. Blaber, D. Bruns, and J. Rottler, Connected network model for the mechanical loss of amorphous materials, Proc. Natl. Acad. Sci. USA **123**, e2513161123 (2025).

[40] A. P. Bartók, J. Kermode, N. Bernstein, and G. Csányi, Machine learning a general-purpose interatomic potential for silicon, Phys. Rev. X **8**, 041048 (2018).

[41] J. D. Morrow and V. L. Deringer, Indirect learning and physically guided validation of interatomic potential models, J. Chem. Phys. **157**, 104105 (2022).

[42] E. Sanscartier, F. Saint-Denis, K.-É. Bolduc and Normand Mousseau, Evaluating approaches for on-the-fly machine learning interatomic potentials for activated mechanisms sampling with the activation-relaxation technique nouveau, J. Chem. Phys. **158**, 244110 (2023).

[43] R. Girard *et al.*, An activation-relaxation technique study of two-level system impact on internal dissipation using DFT-based moment tensor potential, https://doi.org/10.5683/SP3/2621WR, Borealis, V1 (2026).